Proceedings of 2024 IEEE
International Conference on Mechatronics and Automation
August 4 - 7, Tianjin, China

Influence of Materials on the Transportation Performance of a Self-running Actuator Based on Ultrasonic Levitation

Yuanyuan Liu[1,2*], *Jiasheng Shi*[1], *Liang Zhang*[1], *Feng Xie*[1]
[1]*School of Electrical Engineering and Automation, Anhui University*
Jiulong Road No. 111, Hfei, 230601, China
[2]*Anhui Hongqiao Metal Manufacturing Co.. Ltd, Xuancheng, 242300, China*
[*]yuanyuan.liu@ahu.edu.cn, jiasheng_shi@163.com, liangzhang@ahu.edu.cn, Jeexf199@163.com

2024 IEEE International Conference on Mechatronics and Automation (ICMA) | 979-8-3503-8807-7/24/$31.00 ©2024 IEEE | DOI: 10.1109/ICMA61710.2024.10632908

***Abstract* - Ultrasonic levitation (UL) technique holds promising application prospects in the field of actuators due to its oil-free operation, compact structure, and ease of control. This study explores the transportation performance capabilities of a self-running, non-contact actuator utilizing the UL principle, focusing on performance evaluation and material optimization. Initially, the distribution of vibration amplitude was determined using the Finite Element Method (FEM), facilitating the estimation of film thickness. Subsequently, governing equations pertaining to squeeze film pressure were formulated. Incorporating the film thickness and governing equations, air film pressure distribution was ascertained through the Finite Difference Method (FDM). The levitation and driving forces were then calculated based on the force analysis. Furthermore, this paper delves into the impact of the actuator's material on its transportation efficiency. Prediction results show that aluminum yields a higher driving force than titanium at the same input voltage, but titanium surpasses aluminum in generating propulsive force at equivalent amplitude levels. This investigation underscores the significance of material selection in enhancing the performance of UL-based actuators.**

Index Terms - Ultrasonic levitation; material optimization; film pressure; driving force

I. INTRODUCTION

When a radiator operates at ultrasonic frequencies, it induces vibrations that can levitate objects positioned above it by tens to hundreds of microns. This phenomenon is known as Ultrasonic Levitation (UL) [1, 2]. Compared to other levitation technologies, such as magnetic levitation [3] and air cushion levitation [4], UL does not impose material constraints on the levitated object nor does it necessitate an external air supply. Therefore, UL systems have great potential in the field of positioning and transporting fragile and surface-sensitive precision components [5-7]. UL uses ultrasonic frequency vibration to squeeze the air between the radiator and the suspended object, causing the average air pressure in the squeeze film to be greater than the surrounding air pressure, thereby generating a levitation force [8]. Furthermore, should the pressure field within this squeeze film become asymmetric, it can induce driving forces attributable to the viscous properties of the air [9].

Hashimoto *et al.* [10] pioneered the application of Ultrasonic Levitation (UL) technology for non-contact transportation, employing two Langevin transducers to induce travelling wave vibrations in a duralumin plate. Based on this, some researchers have tried to extend its application, such as transporting objects with diverse cross-sectional shapes [11, 12], as well as enhancing the efficiency of such transportation systems [13]. Distinct from the dual-vibration source systems delineated in [10-13], Hu *et al.* [14, 15] introduced an innovative transportation system utilizing a singular vibration source. This system mainly uses asymmetric amplitude distribution to generate asymmetric pressure distribution, thereby generating driving force. In addition, Liu *et al.* [16] presented a transportation system with multiple vibration sources for cylindrical objects by leveraging engraved grooves to disrupt the symmetry of the standing wave acoustic field.

In general, all of the aforementioned transportation systems [10-16] have an obvious characteristic of needing guide rails to generate driving forces. To minimize the space occupied, Koyama *et al.* [17] developed a self-running actuator devoid of the need for guide rails. This actuator distinguishes itself by not only levitating autonomously but also generating its own driving force, demonstrating significant potential for applications in environments where strong magnetic fields or stringent cleanliness are required. Building upon this advancement, Feng *et al.* [18] established a numerical model for this linear actuator and analyzed the effects of amplitude and frequency on its carrying capacity as well as the effect of standing wave ratio (SWR) on its transport capacity. However, the corresponding optimization of structural parameters is not given, which is very important for its performance improvement. Accordingly, in this study, an attempt has been made to study the effect of different materials, namely aluminum (AL2024) and titanium alloy (TiV4) on the transportation performance of this actuator. Parametric analyses on the influences of temporal phase difference and vibration amplitude on transportation performances were also presented.

II. FINITE ELEMENT MODEL

Figure 1 illustrates the schematic diagram and dimensional parameters of the self-running actuator proposed by [17]. This device is primarily comprised of a rectangular frame, augmented on each side by two sets of piezoelectric (PZT) ceramic units. Each set of PZT units incorporates two PZT plates, oriented with opposing polarization directions. When the voltages applied to these two PZT units have a temporal phase difference of θ, the beam on the rectangular frame vibrates according to the inverse piezoelectric effect. Both the wavelength and the direction of the beam vibration can be regulated through adjustments in the phase difference θ

and voltage frequency f. Specifically, a phase difference of θ=0º results in the formation of a standing wave along the beam, initiated by inversely directed waves of equal amplitude from the PZT units at both ends. In this state, the actuator can be suspended but cannot move horizontally. In the remaining cases, i.e., θ is not equal to 0º, the beam will vibrate in the waveform of a travelling wave. Thus, this actuator can move itself in the direction opposite to the direction of the travelling wave [17].

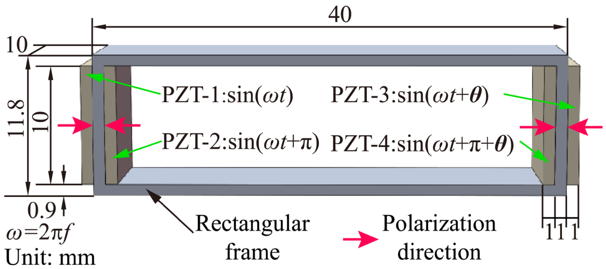

Fig. 1 Configuration and dimensional parameters of the actuator.

To characterize the travelling wave characteristics under different materials, the finite element method (FEM) is employed to analyse the beam's vibratory behaviour. Given the beam's significantly greater length relative to its width (a ratio of 4), it is reasonable to disregard vibrations along the width. In addition, due to the symmetry of the rectangular frame in the height direction, it can be simplified to a one-half symmetric model to reduce the computational cost. Based on the above assumptions, a simplified forced vibration finite element model of the actuator is presented by adhering to Euler-Bernoulli beam theory, as illustrated in Fig. 2. The material properties for the self-running actuator are listed in table Ⅰ.

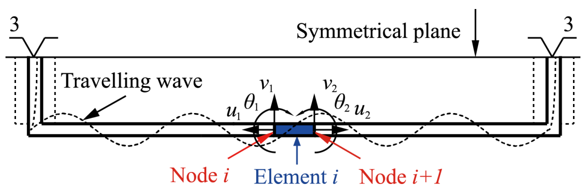

Fig. 2 One-half finite element model of the actuator.

TABLE Ⅰ
MATERIAL PROPERTIES OF THE SELF-RUNNING ACTUATOR

Properties	Rectangular frame		PZT
Material	Aluminum (AL2024)	Titanium alloy (TiV4)	C-213
Density (Kg/m³)	2700	4430	7800
Poisson's ratio	0.33	0.34	0.3
Modulus of elasticity (GPa)	70.3	113.8	82
Weight (N)	0.024	0.039	0.031

The damping effect of the actuator is considered negligible due to its minimal impact [19]. Hence, the governing equation on the vibration deformation of the beam in the global coordinate system is expressed as

$$[M]^G\{\ddot{\xi}\}+[K]^G\{\xi\}=\{F\}^G, \tag{1}$$

where $[M]^G$ and $[K]^G$ are the global mass and stiffness matrix obtained by the node number integration method. The terms $\{\xi\}$ and $\{F\}$ correspond to the distribution of vibration amplitude along the beam and the force engendered via the inverse piezoelectric effect, respectively.

III. GOVERNING EQUATIONS

A. *Film thickness*

To elucidate the transportation performances of the actuator, the analytical model and the corresponding coordinate system are delineated in Fig. 3. As mentioned in Sec. 2, the vibration amplitude distribution is related only to the length direction and not to the width direction, and is symbolized as $\xi(x,t)$. When voltages with different phases are applied to the two groups of PZT units at the ends of the rectangular frame, two travelling waves with different directions and amplitudes will be generated, thereby yielding a mixed wave on the beam, and its expression is written as

$$\xi(x,t)=\xi_m\left[a_1\sin\left(\omega t-\frac{2\pi x}{\lambda}\right)+a_2\sin\left(\omega t+\frac{2\pi x}{\lambda}\right)\right]. \tag{2}$$

In here, ξ_m, $\omega=2\pi f$, and λ are the maximum amplitude, angular frequency of vibration, and the wavelength of the mixed wave, respectively. a_1 and a_2 represent the normalized amplitude of the travelling waves generated by two PZT units, respectively. Therefore, this mixed wave is a combination of travelling and standing waves. The standing wave ratio (SWR), equals $|a_1+a_2|/|a_1-a_2|$, used to characterize the proportion of standing waves in a mixed wave. An SWR value of 1 indicates a purely travelling wave, whereas higher SWR values suggest a predominance of standing wave characteristics. The mean film thickness over one vibration period is represented by h_0. Therefore, the film thickness is

$$h(x,t)=h_0+\xi_m\left[a_1\sin\left(\omega t-\frac{2\pi x}{\lambda}\right)+a_2\sin\left(\omega t+\frac{2\pi x}{\lambda}\right)\right]. \tag{3}$$

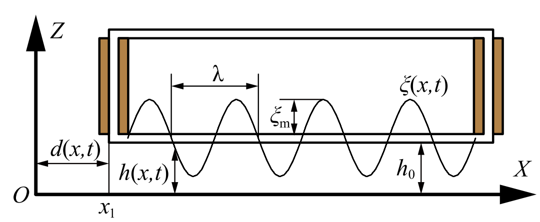

Fig. 3 Analytical model and the corresponding coordinate system of the actuator.

B. *Reynolds Equation*

Many researchers have used the nonlinear Reynolds equation to describe the film pressure resulting from the squeeze action [20-22]. The Reynolds equation is derived from Navier-Stokes equations and the continuity equation. Therefore, some of the assumptions used need to be given here. Firstly, air is treated as a compressible and Newtonian fluid. Secondly, the air pressure gradient in the thickness direction is zero [23]. Thirdly, body and inertia forces of air are disregarded [24]. Fourth, no relative slip occurs at the film-actuator interface [25]. Fifth, the squeeze film is assumed to be isothermal [26]. Consequently, the Reynolds equation considering the horizontal movement of the actuator is stated as [18]

$$\frac{\partial}{\partial x}\left(PH^3\frac{\partial P}{\partial X}\right)+\frac{\partial}{\partial Y}\left(PH^3\frac{\partial P}{\partial Y}\right) = \sigma\frac{\partial(PH)}{\partial T}+\Lambda_v\frac{\partial(PH)}{\partial X}+\Lambda_a\frac{\partial\left(P^2H^3\right)}{\partial X}, \tag{4}$$

where $P = p/p_a$, $H = h/h_0$, $X = x/L$, $Y = y/(L\cdot D)$, and $T = \omega t$ are dimensionless film pressure, film thickness, position in *x*-direction, position in *y*-direction, and time, respectively. L and D are the length and width of the actuator in the *x*- and *y*-directions, respectively. $\sigma = 12\mu_a\omega L^2/p_a h_0^2$ is squeeze number represents the effect of the squeeze effect on the air pressure. Coefficients $\Lambda_v = 6\dot{d}\mu_a L^2/p_a h_0^3$ and $\Lambda_a = -\ddot{d}\rho_a L/2p_a$ stands for the effect of the relative velocity and acceleration in the *x*-direction on the film pressure, respectively. μ_a and ρ_a are the ambient air dynamic viscosity and density, respectively. d is the displacement of the actuator in the *x*-direction relative to its initial position.

In order to maintain the pressure continuity at the interface Γ between the squeeze film and ambient air, the film pressure in this interface satisfies

$$P(\Gamma)=1, \tag{5}$$

in which Γ is composed of four boundary surfaces, i.e., $x = x_1$, $x = x_1 + L$, $y = 0$, and $y = D$. Moreover, the film pressure in the initial time meets

$$P(T=0)=1. \tag{6}$$

Combining the above (3)-(6), the air film pressure variation can be solved using the finite difference method (FDM) and the Newton-Rapson method.

C. Force analysis

There are two kinds of forces originated from the squeeze film. The first one is the levitation force F_L which is used to counteract the weight of the actuator. The second one is the driving force F_D that transports the actuator. After the film pressure P is obtained, the levitation force is the integral of the pressure over the squeeze domain, which is calculated by

$$F_L = \frac{1}{2\pi}\int_0^{2\pi}\int_0^{D}\int_{x_1}^{x_1+L}(P-1)\cdot p_a\,dxdydT. \tag{7}$$

It is noted that F_L is the mean levitation force over one squeeze period, not the transient levitation force. When the actuator is working, it is in a suspended state, so the levitation force and weight are satisfying

$$F_L - mg = 0, \tag{8}$$

where m is the mass of the actuator, and g is the gravitational acceleration.

Since the mixed wave is a mixture of standing and traveling waves, this indicates that the air pressure is asymmetrical in the *x*-direction. Moreover, the horizontal movement of the actuator also affects the air pressure gradient. As a result, a shear stress acting on the bottom surface of the actuator is developed, and expressed by [18]

$$\tau_{zx}\big|_{(z=h)} = \frac{h}{2}\frac{\partial p}{\partial x}+\mu_a\frac{\dot{d}}{h}+\frac{\rho h\ddot{d}}{3}, \tag{9}$$

where ρ is the film density. Integrating the shear force over the squeeze domain gives the driving force. The mean driving force for one squeeze period is written as

$$F_D = \frac{1}{2\pi}\int_0^{2\pi}\int_0^{D}\int_{x_1}^{x_1+L} -\left(\frac{h}{2}\frac{\partial p}{\partial x}+\mu_a\frac{\dot{d}}{h}+\frac{\rho h\ddot{d}}{3}\right)dxdydT. \tag{10}$$

Since the normal to the bottom of the actuator is in the z-negative direction, a negative sign needs to be added to the right side of (10). In this study, since the actuator is stationary during the measurement of the driving force [17], the air drag force is negligible and the displacement d is zero.

IV. Results and Discussions

A. Amplitude distribution

Under the excitation parameters of voltage at 40 $V_{p\text{-}p}$, frequency f at 100 kHz, and a temporal phase difference θ of 135º, the amplitude distribution along the beam of the actuator, was measured using a laser Doppler vibrometer (CLV-1000 and 700, PI Polytec, Waldbronn, Germany), as displayed in Fig. 4(a). The rectangular frame fabricated from AL2024 material. The experimental data in [17] represented by circular dots, indicate that the actuator operates in the eighth order of flexural vibration mode.

Under the same conditions, using the forced vibration model shown in Fig. 1, the numerical amplitude distribution of the beam can be obtained by solving (1), as shown by the solid line in Fig. 4(a). It can be found that the numerical results compare well with the experimental results, which verifies the correctness of the finite element model proposed in this paper. Moreover, the propagation direction of the mixed wave, moving from the right end to the left end of the beam, is portrayed in Fig. 4(b). Meanwhile, the maximum amplitude ξ_m varies over time, attributed to the composite nature of the wave, encompassing both standing and traveling wave components. The coefficients a_1, a_2, and the wavelength λ in (2) are 0.148, 0.882, and 0.6664, respectively.

B. Pressure distribution

In subsequent analyses, the same operating conditions and parameters as in the previous subsection were maintained, but the voltage was set to 80 $V_{p\text{-}p}$. The ambient air satisfies the following properties: density ρ_a =1.204 kg/m³, pressure p_a =1.013×10⁵ Pa, and dynamic viscosity μ_a =1.81×10⁻⁵ Pa·s. The weight of the actuator is 0.055 N. The squeeze domain is equal to the area of the bottom surface of the actuator, which is divided into 80 and 20 meshes in the length and width directions, respectively. The computed pressure distribution along the midline (y=D/2) during one steady squeeze period, presented in Fig. 5, reveals that the air pressure waveform progresses in the x-positive direction, counter to the traveling wave's direction shown in Fig. 4(b). Therefore, this actuator can move to the right because the dynamic viscosity of the air produces a driving force to the right. Since the vibration waveform on the beam is not a pure traveling wave, but a superposition of standing and traveling waves, the peak value of the air pressure changes at different moments. Since the SWR is 1.36, indicating that the wave behaves very much like a pure traveling wave, the peak air pressure exhibits minimal changes.

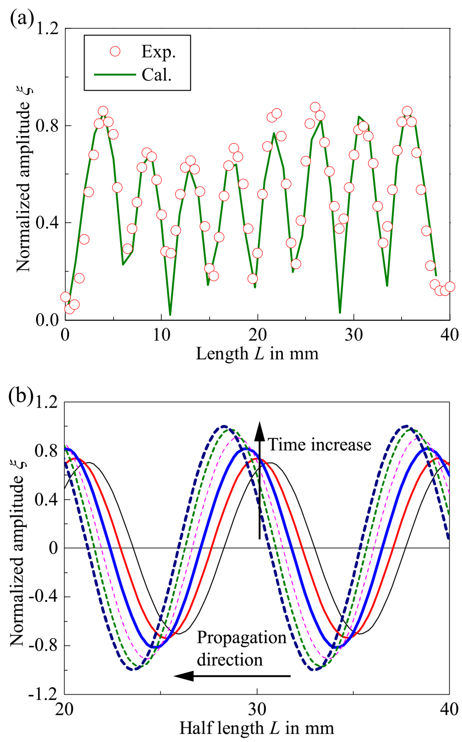

Fig. 4 (a) Comparison of normalized amplitude distribution results acquired by experiment and calculation; (b) Variation of the normalized amplitude distribution along the half length of the beam during a quarter period.

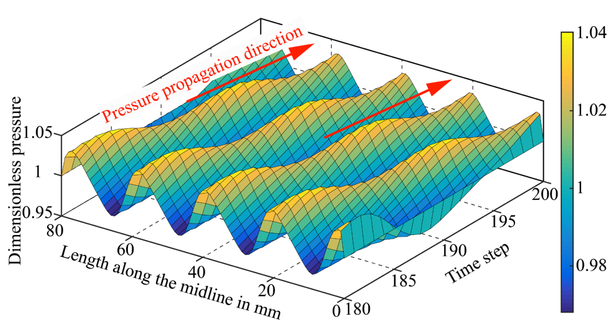

Fig. 5 Dimensionless pressure distribution on the middle line in the width direction over one period at θ=135º.

C. Transportation Performance

Controlling the variation of the temporal phase difference θ gives its relationship to the driving force F_D. Specify that the driving force is positive when it is in the same direction as the x-positive direction. With the excitation voltage and frequency configured at 80 $V_{\text{p-p}}$ and 100 kHz respectively, and all other parameters held constant, Figure 6(a) illustrates the relationship between the driving force and the phase difference for two distinct materials, AL2024 and TiV4. Numerical results for AL2024 and TiV4 are shown in heavy and thick solid lines, respectively. In addition, to affirm the accuracy of these calculations, the experimental results [17] for AL2024, denoted by triangle dots, are also provided. It can be found that the driving force remains positive as θ ranges from 0° to 180°, and becomes negative as θ extends from 180° to 360°, delineating a sinusoidal-like dependency on the phase angle. The congruence between numerical and experimental data under identical materials validates the model proposed in this paper. In addition, the driving force for AL2024 is higher than that for TiV4. This is because, at the same excitation voltage, the amplitude of TiV4 is smaller because of its larger elastic modulus. Conversely, when the maximum amplitude is the same, TiV4 demonstrates a superior driving force compared to AL2024, as depicted in Fig. 6(b). This is because the larger weight of TiV4 results in a smaller thickness of the squeeze film, thereby enhancing the squeeze effect. Likewise, increasing the amplitude leads to an increase in the driving force.

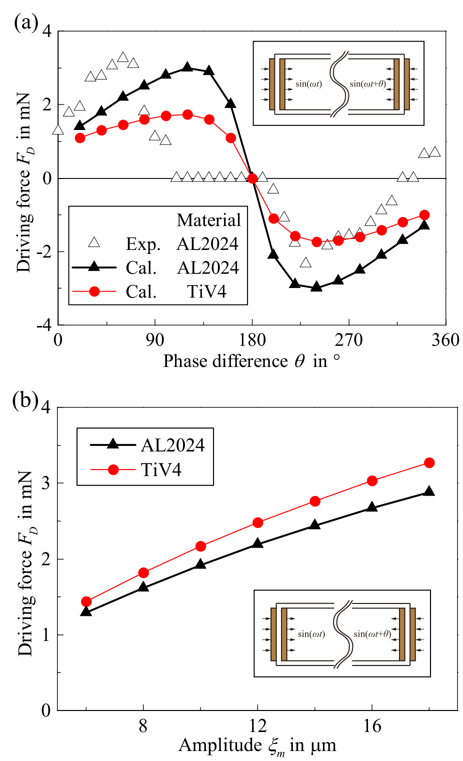

Fig. 6 Driving force versus (a) phase difference and (b) maximum amplitude for AL2024 and TiV4.

V. Conclusions

This study initially formulates a simplified finite element model of forced vibration for a self-running actuator and proceeds to calculate its amplitude distribution. Subsequently, the Reynolds equation is employed to calculate the air film pressure distribution using the finite difference method (FDM) and Newton-Raphson method. Through the force analysis, both the levitation and driving forces are computed. The numerical model presented in this paper is validated by comparing the experimental and computational results under the same conditions. Finally, the parametric analysis unveils a sinusoidal-like interdependence between the driving force and the phase difference. Notably, AL2024 produces a higher driving force under the same excitation voltage, whereas TiV4 excels in driving force generation under identical maximum amplitude conditions. Future endeavours will be directed towards optimizing the structural parameters of this actuator to enhance its performance further.

Acknowledgment

This research was supported by the National Natural Science Foundation of China (NSFC) under Grant No. 52305173 and the Key Program Foundation of Department of Education, Anhui Province, China under Grant No. 2023AH050079.

References

[1] R. R. Whymark, “Acoustic field positioning for containerless processing,” Ultrasonics, vol. 13, no. 6, pp. 251-261, 1975.

[2] G. Chen, W. Zhang, Z. Chen, and S. Tang, “Optimization of ultrasonic levitation bearing load characteristics based on rotor surface microstructure,” Physics of Fluids, vol. 35, no. 12, pp. 126113, 2023.

[3] H. Zhang, Y. X. Lou, L. S. Zhou, Z. Q. Kou, and J. R. Mu, “Modeling and optimization of a large-load magnetic levitation gravity compensator,” IEEE Transactions on Industrial Electronics, vol. 70, no. 5, pp. 5055-5064, MAY. 2023.

[4] G. J. Laurent, A. Delettre, and N. Le Fort-Piat, “A new aerodynamic-traction principle for handling products on an air cushion,” IEEE Transactions on Robotics, vol. 27, no. 2, pp. 379-384, APR. 2011.

[5] S. Ueha, Y. Hashimoto, and Y. Koike, “Non-contact transportation using near-field acoustic levitation,” Ultrasonics, vol. 38, no. 1, pp. 26-32, 2000.

[6] V. Vandaele, P. Lambert, and A. Delchambre, “Non-contact handling in microassembly: Acoustical levitation,” Precision Engineering, vol. 29, no. 4, pp. 491-505, 2005.

[7] Y. Y. Liu, M. H. Shi, K. Feng, K. K. Sepahvand, and S. Marburg, “Stabilizing near-field acoustic levitation: Investigation of non-linear restoring force generated by asymmetric gas squeeze film,” The Journal of the Acoustical Society of America, vol. 148, no. 3, pp. 1468-1477, 2020.

[8] T. A. Stolarski, and C. Wei, “Load-carrying capacity generation in squeeze film action,” International Journal of Mechanical Sciences, vol. 48, no. 7, pp. 736-741, 2006.

[9] Y. Koike, S. Ueha, A. Okonogi, T. Amano, and K. Nakamura, “Suspension mechanism in near field acoustic levitation phenomenon,” in 2000 IEEE International Ultrasonics Symposium, San Juan, USA, 2000, pp. 671-674.

[10] Y. Hashimoto, Y. Koike, and S. Ueha, “Transporting objects without contact using flexural traveling waves,” The Journal of the Acoustical Society of America, vol. 103, no. 6, pp. 3230-3233, 1998.

[11] T. Ide, J. Friend, K. Nakamura, and S. Ueha, “A non-contact linear bearing and actuator via ultrasonic levitation,” Sensors and Actuators A: Physical vol. 135, no. 2, pp. 740-747, 2007.

[12] D. Koyama, T. Ide, J. R. Friend, K. Nakamura, and S. Ueha, “An ultrasonically levitated noncontact stage using traveling vibrations on precision ceramic guide rails,” IEEE Transactions on Ultrasonics, Ferroelectrics, and Frequency control, vol. 54, no. 3, pp. 597-604, 2007.

[13] J. F. Liu, H. Jiang, H. You, X. Y. Jiao, H. X. Chen, and G. J. Liu, “Non-contact transportation of heavy load objects using ultrasonic suspension and aerostatic suspension,” Proceedings of the Institution of Mechanical Engineers, Part C: Journal of Mechanical Engineering Science, vol. 228, no. 5, pp. 840-851, 2014.

[14] J. H. Hu, G. R. Li, H. L. W. Chan, and C. L. Choy, “A standing wave-type noncontact linear ultrasonic motor,” IEEE Transactions on Ultrasonics, Ferroelectrics, and Frequency Control, vol. 48, no. 3, pp. 699-708, 2001.

[15] J. H. Hu, K. C. Cha, and K. C. Lim, “New type of linear ultrasonic actuator based on a plate-shaped vibrator with triangular grooves,” IEEE Transactions on Ultrasonics, Ferroelectrics, and Frequency Control, vol. 51, no. 10, pp. 1206-1208, 2004.

[16] Y. Y. Liu, M. Eser, X. D. Sun, K. K. Sepahvand, and S. Marburg, “Theoretical analysis of a contactless transportation system for cylindrical objects based on ultrasonic levitation,” The Journal of the Acoustical Society of America, vol. 150, no. 3, pp. 1682-1690, 2021.

[17] D. Koyama, K. Nakamura, and S. Ueha, “A stator for a self-running, ultrasonically-levitated sliding stage,” IEEE Transactions on Ultrasonics, Ferroelectrics, and Frequency Control, vol. 54, no. 11, pp. 2337-2343, 2007.

[18] K. Feng, Y. Y. Liu, and M. M. Cheng, “Numerical analysis of the transportation characteristics of a self-running sliding stage based on near-field acoustic levitation,” The Journal of the Acoustical Society of America, vol. 138, no. 6, pp. 3723-3732, 2015.

[19] A. Almurshedi, M. Atherton, C. Mares, and T. A. Stolarski, “Modelling influence of Poisson's contraction on squeeze film levitation of planar objects,” Journal of Applied Physics, vol. 125, no. 9, pp. 095303, 2019.

[20] W. J. Li, Y. Y. Liu, and K. Feng, “Modelling and experimental study on the influence of surface grooves on near-field acoustic levitation,” Tribology International, vol. 116, pp. 138-146, 2017.

[21] H. Li, and Z. Q. Deng, “Prediction of load-carrying capacity in the radial direction for piezoelectric-driven ultrasonic bearings,” IEEE Access, vol. 7, pp. 30599-30614, 2019.

[22] P. K. Liu, J. Li, H. Ding, and C. W. W., “Modeling and experimental study on near-field acoustic levitation by flexural mode,” IEEE Transactions on Ultrasonics, Ferroelectrics, and Frequency Control, vol. 56, no. 12, pp. 2679-2685, 2009.

[23] A. Minikes, and I. Bucher, “Noncontacting lateral transportation using gas squeeze film generated by flexural traveling waves-numerical analysis,” The Journal of the Acoustical Society of America, vol. 113, no. 5, pp. 2464-2473, 2003.

[24] T. A. Stolarski, and W. Chai, “Self-levitating sliding air contact,” International Journal of Mechanical Sciences, vol. 48, no. 6, pp. 601-620, 2006.

[25] Y. Y. Liu, X. D. Sun, Z. L. Zhao, H. H. Zeng, and W. J. Chen, “Stability analysis of near-field acoustic levitation considering misalignment and inclination,” International Journal of Mechanical Sciences, vol. 265, pp. 108901, 2024.

[26] A. Minikes, and I. Bucher, “Comparing numerical and analytical solutions for squeeze-film levitation force,” Journal of Fluids and Structures, vol. 22, no. 5, pp. 713-719, 2006.